Variability of the Atlantic Meridional Overturning Circulation in CCSM4

Gokhan Danabasoglu and Steve G. Yeager

National Center for Atmospheric Research, Boulder, Colorado

Young-Oh Kwon

Woods Hole Oceanographic Institution, Woods Hole, Massachusetts

Joseph J. Tribbia, Adam S. Phillips, and James W. Hurrell

National Center for Atmospheric Research, Boulder, Colorado

ABSTRACT

Atlantic meridional overturning circulation (AMOC) variability is documented in the Community Climate System Model, version 4 (CCSM4) preindustrial control simulation that uses nominal 1° horizontal resolution in all its components. AMOC shows a broad spectrum of low-frequency variability covering the 50–200-yr range, contrasting sharply with the multidecadal variability seen in the T85 × 1 resolution CCSM3 present-day control simulation. Furthermore, the amplitude of variability is much reduced in CCSM4 compared to that of CCSM3. Similarities as well as differences in AMOC variability mechanisms between CCSM3 and CCSM4 are discussed. As in CCSM3, the CCSM4 AMOC variability is primarily driven by the positive density anomalies at the Labrador Sea (LS) deep-water formation site, peaking 2 yr prior to an AMOC maximum. All processes, including parameterized mesoscale and submesoscale eddies, play a role in the creation of salinity anomalies that dominate these density anomalies. High Nordic Sea densities do not necessarily lead to increased overflow transports because the overflow physics is governed by source and interior region density differences. Increased overflow transports do not lead to a higher AMOC either but instead appear to be a precursor to lower AMOC transports through enhanced stratification in LS. This has important implications for decadal prediction studies. The North Atlantic Oscillation (NAO) is significantly correlated with the positive boundary layer depth and density anomalies prior to an AMOC maximum. This suggests a role for NAO through setting the surface flux anomalies in LS and affecting the subpolar gyre circulation strength.

1. Introduction

The Atlantic meridional overturning circulation (AMOC) is thought to play an important role in decadal and longer time-scale climate variability as well as in prediction of the earth's future climate on these time scales. Through its associated heat and salt transports, AMOC significantly influences the climate of the North Atlantic and surrounding areas. In particular, changes in sea surface temperatures (SSTs) linked to AMOC variability can impact even global climate through atmospheric interactions on interannual and (multi)decadal time scales

(see Sutton and Hodson 2005; Hurrell et al. 2006, and references therein). However, because only a rather short record of continuous observational estimates of AMOC transports is available, that is, only since 2004 [Rapid Climate Change (RAPID) mooring array; Cunningham et al. (2007)], support for such a prominent role for AMOC primarily comes from coupled general circulation model (CGCM) simulations, many of which show rich variability of AMOC particularly on decadal and longer time scales (e.g., Delworth et al. 1993). Specifically, various AMOC index time series tend to lead the SST changes in CGCMs, thus providing a rather casual evidence of AMOC's *driving* influence. This argument is also invoked to associate the low-frequency fluctuations (with a 40–70-yr period range) of the Atlantic multidecadal variability (AMV) with changes in AMOC. The AMV represents an index of the *observed* Atlantic SST variability estimated

Corresponding author address: Gokhan Danabasoglu, National Center for Atmospheric Research, P.O. Box 3000, Boulder, CO 80307.
E-mail: gokhan@ucar.edu

from instrumental records and proxy data (e.g., Schlesinger and Ramankutty 1994; Kushnir 1994; Delworth and Mann 2000).

Until longer and denser AMOC observations become available, CGCMs along with simpler process models will necessarily remain as the main tools to study AMOC variability and its mechanisms. Unfortunately, CGCMs exhibit a wide range of AMOC variability with important differences in peak periods and amplitudes among them (see, e.g., Danabasoglu 2008; Kwon and Frankignoul 2012 for summaries of previous work). Furthermore, the proposed AMOC variability mechanisms are largely model dependent and are not robust across different models. In addition to the atmosphere and ocean model resolutions (Bryan et al. 2006), the period and amplitude of AMOC variability are shown to be affected by some oceanic subgridscale parameterizations, for example, magnitude of vertical diffusivity coefficients (Farneti and Vallis 2011) and representation of the Nordic Sea overflows (Yeager and Danabasoglu 2012). Despite these challenges, interest in AMOC variability remains high for two reasons: a desire to find a robust variability mechanism and for providing appropriate ocean initial conditions used for decadal prediction experiments. The latter is due to suggested potential predictability associated with AMOC and upper-ocean temperatures on decadal time scales (e.g., Griffies and Bryan 1997; Pohlmann et al. 2004; Msadek et al. 2010; Branstator and Teng 2010).

As in other CGCMs, the present-day control simulations of the previous version of the Community Climate System Model, version 3 (CCSM3) exhibited rich AMOC variability. CCSM3 had three different resolution versions: T85 × 1 [T85 (about 1.4°) and nominal 1°]; T42 × 1 [T42 (about 2.8°) and nominal 1°]; and T31 × 3 [T31 (about 3.75°) and nominal 3°] where the first and second numbers indicate atmosphere and ocean model horizontal resolutions, respectively. The sensitivity of AMOC variability to changes in resolution was presented in Bryan et al. (2006), which showed that AMOC variability amplitude increases with increasing overall resolution. With its largest AMOC amplitude, T85 × 1 had two distinct AMOC variability regimes: a 300-yr-long oscillatory regime with a period of 21 yr followed by much weaker irregular variability regime with a broad variance maximum at a period of about 40 yr. The first regime was analyzed in Danabasoglu (2008) and the North Atlantic Oscillation (NAO) was found to play a prominent role in modulating the subpolar gyre strength and the properties in the model's deep-water formation (DWF) region near the Labrador Sea (LS), thus implying an air–sea coupled mode. Kwon and Frankignoul (2012) found resemblance in the climatologies and dominant modes of variability between the two regimes. They reported

only minor differences in the subpolar gyre circulation in the second regime compared to the first one, but indicated that even slight differences may lead to distinctly different AMOC behavior. Furthermore, there was less evidence for an atmosphere–ocean coupled mode, but a role for oceanic advection of density anomalies into the DWF site. Nevertheless, NAO was still involved in the subpolar gyre changes. In T42 × 1, Teng et al. (2011) identified a dominant variability range of 10–30 yr (centered around 20 yr) and suggested links with NAO. As for T31 × 3, while Danabasoglu (2008) reported a significant peak at centennial time scales using a 500-yr time series, D'Orgeville and Peltier (2009) characterized AMOC variability as broad spectrum of low frequencies with no significant peaks, considering a 300-yr time series from a different simulation. They also showed a 60-yr AMOC peak from a T31 × 3 preindustrial control experiment, indicating that AMOC variability also depends on the control simulation. This latter variability was explained as an interaction between the subpolar gyre circulation and bottom bathymetry with NAO excluded as the leading driving mechanism.

The newest version of the CCSM, CCSM4, has been recently released to the community. As discussed in Gent et al. (2011), the primary CCSM4 control integration is a 1300-yr preindustrial simulation, performed using the nominal 1° horizontal resolution versions of all the component models. We expect that this long control simulation will be widely utilized by the community. In addition, the same model configuration is used in our decadal prediction experiments, results of which are submitted to the Intergovernmental Panel on Climate Change Fifth Assessment Report. Therefore, we believe that it is important to document the unforced, intrinsic AMOC variability in this control simulation. Consequently, our goal in this study is to provide a detailed analysis of the AMOC variability present in this experiment. Associated variability in other climatically important oceanic and atmospheric fields, such as oceanic heat transport and surface temperatures, are also documented. In addition, the impacts of the Nordic Sea overflows on the AMOC variability are discussed. Finally, we explore mechanisms for model AMOC variability, particularly focusing on the LS region. Wherever relevant, we compare the AMOC-related variability in CCSM4 to those of T85 × 1 CCSM3 simulation introduced above as this CCSM3 simulation was the primary, highest-resolution control experiment used in many studies. The paper is organized as follows. In section 2, we give brief descriptions of the coupled model as well as the CCSM4 and CCSM3 experiments. The results are presented in section 3. Section 4 includes a summary and discussion.

2. Model and experiments

The CCSM4 is a fully coupled model of the earth's physical climate system. Its components are the Community Atmosphere Model version 4 with a finite volume dynamical core [Community Atmosphere Model, version 4 (CAM4); R. B. Neale et al. 2012, unpublished manuscript], the Parallel Ocean Program, version 2 (POP2; Smith et al. 2010); the Community Land Model, version 4 (CLM4; Lawrence et al. 2012); and the Sea Ice Model, version 4 (CICE4; Holland et al. 2012). Gent et al. (2011) give a general description of the CCSM4 and show some results from the preindustrial control and the twentieth-century simulations in comparison with CCSM3. A description of the ocean model, highlighting major developments since CCSM3, along with the solutions from the twentieth-century simulations in comparison with available observations and those of CCSM3 are presented in Danabasoglu et al. (2012). The CCSM4 POP2 includes several new features that are particularly relevant for the present study: i) the representation of the Denmark Strait (DS) and Faroe Bank Channel (FBC) overflows has been significantly improved by incorporating an overflow parameterization (Danabasoglu et al. 2010) based on the marginal sea boundary condition scheme of Price and Yang (1998), ii) the effects of diabatic mesoscale fluxes within the surface diabatic layer are included using a near-surface eddy flux parameterization (Ferrari et al. 2008; Danabasoglu et al. 2008), iii) both the thickness and isopycnal diffusivity coefficients used in the Gent and McWilliams (1990) isopycnal transport parameterization vary identically in the vertical following Ferreira et al. (2005) and Danabasoglu and Marshall (2007), with enhanced diffusivity values in the upper ocean and much smaller diffusivities at depth, and iv) the restratification effects of the finite-amplitude, submesoscale mixed layer eddies are included using the mixed layer eddy parameterization of Fox-Kemper et al. (2008) as implemented by Fox-Kemper et al. (2011).

The CCSM4 1850 preindustrial control experiment was integrated for 1300 yr, using a global- and annual-mean CO_2 mixing ratio of 284.7 ppmv. All component models used their nominal 1° horizontal resolution versions with CLM4 sharing the same grid as CAM4 and CICE4 sharing the same grid as POP2. The coupled simulation was initialized from a preliminary preindustrial integration.

The CCSM3 control simulation considered here was for the 1990 present-day conditions with a global- and annual-mean CO_2 mixing ratio of 355 ppmv. The atmospheric model had a spectral dynamical core with a T85 spectral truncation in the horizontal. The land model was on the same horizontal grid as the atmosphere. The ocean and sea ice models shared the same horizontal grid with a nominal 1° resolution—indeed this grid is identical to the one used in the present CCSM4 experiment. We note however that the ocean model in CCSM3 had only 40 vertical levels as opposed to the 60 levels used in the CCSM4 POP2. Consequently, CCSM3 and CCSM4 ocean configurations differ in their representations of the bottom topography as well as some details of the ocean–land mask. The CCSM3 present-day control was integrated for 700 yr, starting with the January-mean climatological potential temperature and salinity [a blending of Levitus et al. (1998) and Steele et al. (2001) datasets] and zero velocities in the ocean. The remaining components were initialized with January conditions obtained from standalone integrations. Further details of this CCSM3 present-day simulation are given in Collins et al. (2006) and references therein.

We refer to the CCSM4 preindustrial and CCSM3 present-day control simulations simply as CCSM4 and CCSM3, respectively. Our CCSM4 analysis uses the last 600 yr of the simulation, corresponding to years 700 to 1299. This choice avoids the initial period in which the AMOC maximum transport shows a roughly monotonic weakening (see Fig. 1a). We use annual-mean fields in the present study except for the boundary layer depth where March-mean data are utilized. The time-mean distributions for CCSM4 represent 600-yr means for years 700–1299. Standard correlation, regression, spectral analysis, and empirical orthogonal function (EOF) methods are employed. All the time series are detrended using a linear least squares fit prior to analysis. There are a few reasons for our use of annual data in the present study. An analysis using a 30-yr low-pass Lanczos-filtered (Duchon 1979) time series shows very similar results to those obtained just by using the annual time series. Furthermore, low-frequency features of interest are largely absent when a 15-yr high-pass Lanczos filter is applied, indicating that the dominant relationships exhibited by the annual time series are those associated with the low-frequency variability. Lastly, using the annual time series makes the interpretation of lead–lag relationships unambiguous. The EOF time series are normalized to have unit variance, so that the EOF spatial pattern magnitudes correspond to one standard deviation changes in the EOF time series. Reference red noise spectra with the same total variances and the associated 95% confidence level are shown in all related plots. The effective temporal degrees of freedom (DOF) of annual time series are calculated using lag-one serial autocorrelations. When the significance of correlations and regressions are tested between any two time series, a two-sided Student's t test is employed, using the smaller DOF of the two time series. Finally, a 5-point smoothing in frequency domain is applied in spectral plots.
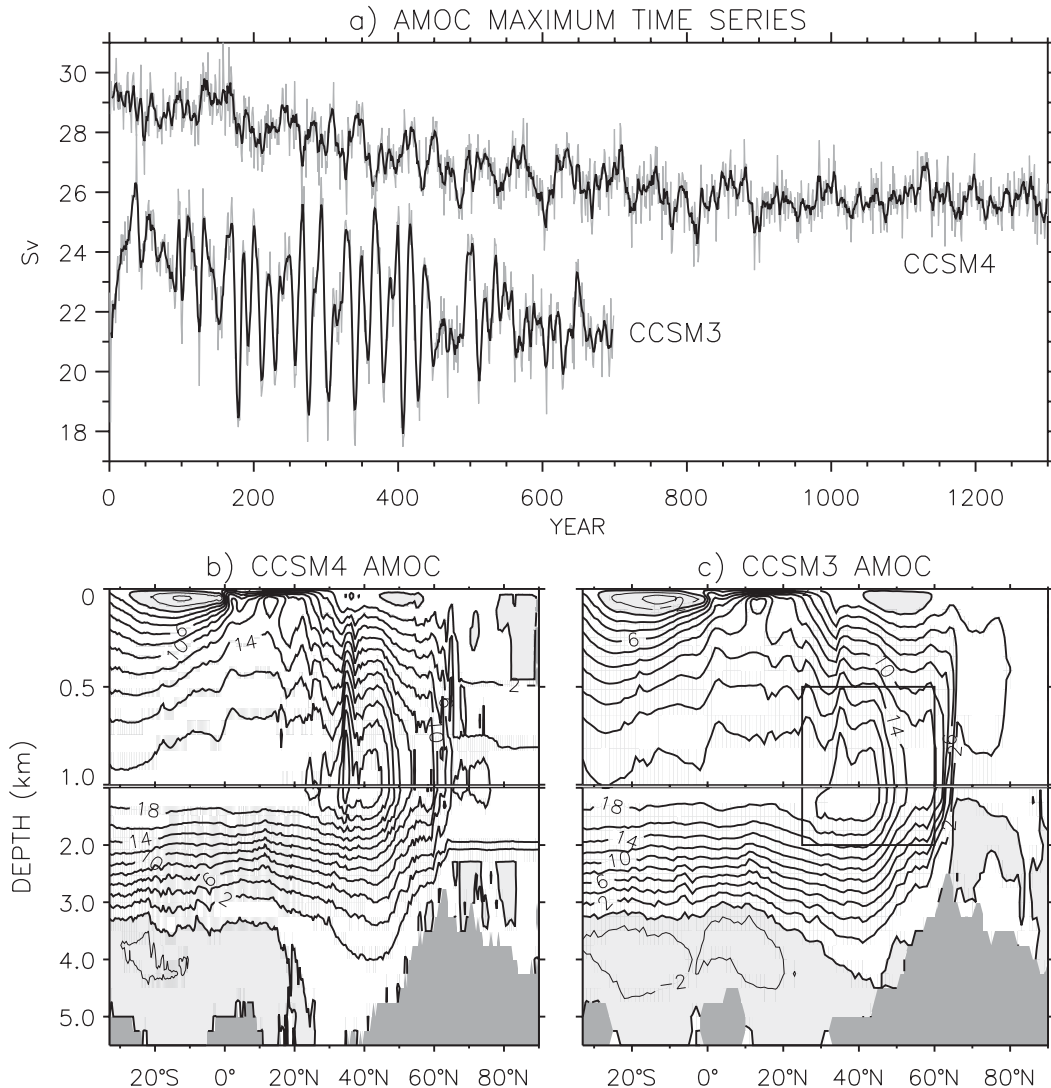
FIG. 1. (a) Annual-mean AMOC maximum transport time series (gray lines) from CCSM4 and CCSM3. The maximum is searched for within the boxed region shown in (c). The black lines represent smoothed time series using a 5-yr running mean. Time-mean AMOC from (b) CCSM4 (yr 700–1299 mean) and (c) CCSM3 (yr 151–450 mean). The contour interval is 2 Sv. The positive (thick lines) and negative (thin lines, shading) contours indicate clockwise and counterclockwise circulation, respectively.

3. Results

a. AMOC mean and variability

We continue to use the AMOC maximum transport and EOF principal component (PC) time series in this study because i) neither of the CCSM3 nor CCSM4 simulations analyzed here shows localized, small-scale AMOC features as described in Yeager and Danabasoglu (2012), and ii) these time series remain associated with large-scale spatial features of AMOC variability. Figure 1a presents the maximum transport time series for CCSM4 and CCSM3. This maximum is searched for within the boxed region shown in Fig. 1c and corresponds to the maximum transport of the circulation associated with the North Atlantic Deep Water (NADW). The CCSM4 time series clearly show two significant differences from those of CCSM3. First, there are no obvious oscillatory regimes as in years 150–450 of CCSM3. Second, the transport variability is much reduced in CCSM4. Indeed, the CCSM4 variance of 0.51 Sv^2 (1 Sv $\equiv$ 10^6 m^3 s^{-1}) for years 700–1299 is much smaller than the CCSM3 variances of 4.24 Sv^2 for years 150–450 (regime I; Danabasoglu 2008) and 1.25 Sv^2 for years 450–699 (regime II; Kwon and Frankignoul 2012). It is unclear which coupled model changes are responsible for this large reduction in AMOC variability as CCSM4 contains many improvements
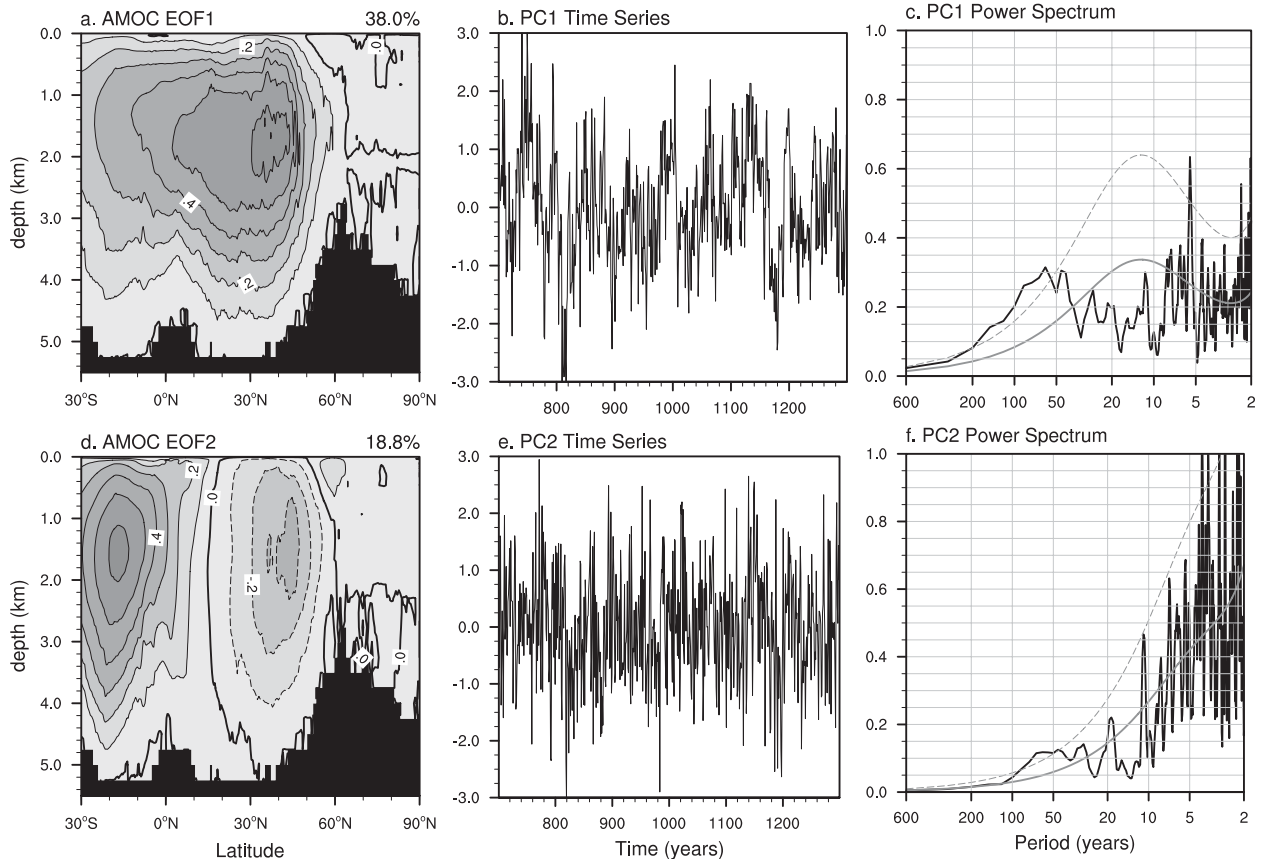
FIG. 2. AMOC EOF1 (a) spatial distribution, (b) time series, and (c) power spectrum. AMOC EOF2 (d) spatial distribution, (e) time series, and (f) power spectrum. In (a),(d), the contour interval is 0.1 Sv and the positive (solid) and negative (dashed) contours indicate clockwise and counterclockwise circulation, respectively. In (c),(f), the reference red noise spectrum with the same total variance is given by the solid gray line and the dashed line shows its 95% confidence limit. The power spectra are presented in a variance preserving form. Also, a 5-point smoothing in frequency is applied to the spectra.

particularly in the ocean model. However, Yeager and Danabasoglu (2012) show that the overflow parameterization used to represent the DS and FBC overflows partly contributes to this reduction in AMOC variance by maintaining stratification in the LS basin. These differences in AMOC variability between CCSM4 and CCSM3 can be also due to their mean state differences, but a recent study by D'Orgeville and Peltier (2009) find that the AMOC maximum transport standard deviations (SD) are identical in preindustrial and present-day T31 × 3 CCSM3 control simulations despite differences in their mean states. Figure 1a also shows a roughly monotonic weakening of the AMOC maximum transport through the first 500–600 yr in CCSM4, in contrast with CCSM3. We further note that the CCSM4 time series do not show a rapid initial increase as it was initialized from a preliminary preindustrial case. Finally, as also revealed by the time-mean AMOC distributions (Figs. 1b and 1c), the NADW has a larger mean transport in CCSM4 than in CCSM3 (25.8 versus 22.0 Sv, respectively). Thus, in

CCSM4, the AMOC SD represents only about 3% of the maximum NADW transport. In contrast, the corresponding AMOC SDs are about 9% and 5% for regime I and regime II, respectively, in CCSM3. We believe that the stronger mean transport in CCSM4 is partly due to its preindustrial conditions as the CCSM4 twentieth-century simulations show a maximum NADW transport reduced to about 24 Sv (Danabasoglu et al. 2012). In CCSM4, the NADW cell penetrates deeper than in CCSM3 north of 30°N due to the overflow parameterization. The circulation associated with the Antarctic Bottom Water (AABW) is particularly anemic in CCSM4.

We show the AMOC EOF1 and EOF2 spatial patterns, time series, and power spectra in Fig. 2. These two EOFs account for 38% and 18.8% of the total AMOC variance, respectively. The first EOF has a single cell pattern, covering the entire Atlantic Basin south of 60°N. In its positive phase, it indicates that the NADW cell gets stronger and penetrates deeper. In contrast, the EOF2 has a dipole structure with an overturning cell between 15°–60°N and
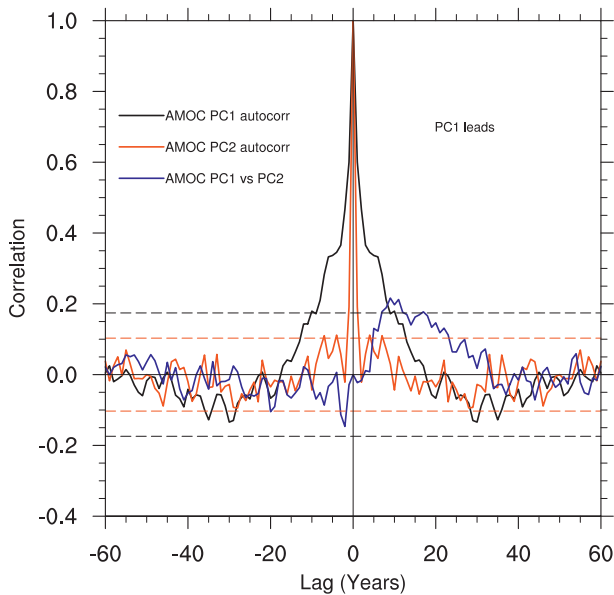
FIG. 3. Autocorrelations of the AMOC PC1 (black) and PC2 (red) time series. The correlation function for the two time series is given by the blue line. The black and red dashed lines show the 95% confidence levels for the PC1 and PC2 time series, respectively. The black dashed line also represents the 95% confidence level for the PC1 and PC2 correlation.

a stronger, opposite circulation south of 15°N (counterclockwise and clockwise circulations, respectively, in Fig. 2d). These EOF1 and EOF2 spatial patterns are very similar to those of CCSM3. However, in CCSM3, EOF1 represented a larger fraction of the total variance and EOF2 had accordingly a smaller fraction than in CCSM4. Low-frequency variability of AMOC is particularly evident in PC1 time series with the associated spectrum showing a broad, statistically significant band for the 50–200-yr range. The PC2 time series also show variability in the 50–100-yr range, but its peak and confidence level are smaller than in PC1. Both PCs reveal substantial interannual variability with particularly larger amplitudes in the PC2 time series. The AMOC PC1 and maximum transport time series are highly correlated with a simultaneous correlation coefficient of 0.74 (>99% confidence level). The correlation remains statistically significant (>99%) at 0.80 when both time series are smoothed using a 5-yr low-pass Lanczos filter. Therefore, we choose to use the PC1 time series as our reference time series in the rest of this study.

The AMOC PC1 autocorrelation function suggests a strongly damped, low-frequency variability (Fig. 3). The minimum correlation occurs at 30–35-yr lags and the second zero crossing is located roughly between 45–60 yr. Variability associated with PC2 appears to be even more strongly damped than in PC1. The correlation function between PC1 and PC2 attains its largest value with 0.22
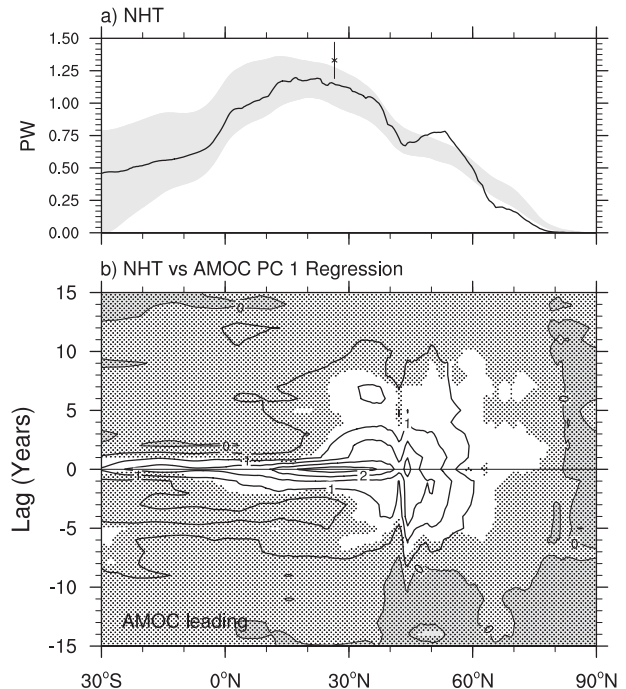

FIG. 4. (a) Time-mean NHT from CCSM4 due to the Eulerian-mean velocity. The shading shows the implied transport range in individual years for the 1984–2006 period from Large and Yeager (2009). The cross with the error bar is an estimate based on the RAPID data from Johns et al. (2011). (b) NHT regression with the AMOC PC1 time series. The regression field is scaled by 100 and the contour interval is 5×10^{-3} PW per AMOC PC1 unit variance. The thin lines and shading indicate negative regions. AMOC PC1 leads for negative lags. No stippling denotes confidence above the 95% level.

when PC1 leads PC2 by about 10 yr, indicating weakening of AMOC strength north of about 15°N. This weakening is partly associated with the impacts of the parameterized overflows on AMOC (see section 3c and Fig. 6 below). The AMOC PC1 and PC2 relationship suggests a southward propagation of the positive AMOC anomalies as also indicated in some other coupled models (e.g., Dong and Sutton 2005; Mignot and Frankignoul 2005; Guemas and Salas-Melia 2008). Although such a propagation is not supported by the annual AMOC time series regressions on to the annual AMOC PC1 time series, it becomes more evident after a 30-yr low-pass Lanczos filter is applied to both time series (not shown).

The time-mean northward heat transport (NHT) in the Atlantic Ocean in this CCSM4 preindustrial control simulation is mostly within the range of implied transport estimates from Large and Yeager (2009) for the 1984–2006 *present-day* period but remains lower than the estimate range based on the RAPID data from Johns et al. (2011) at 26.5°N (Fig. 4a). The maximum transport of 1.19 PW occurs between 17°–23°N. The
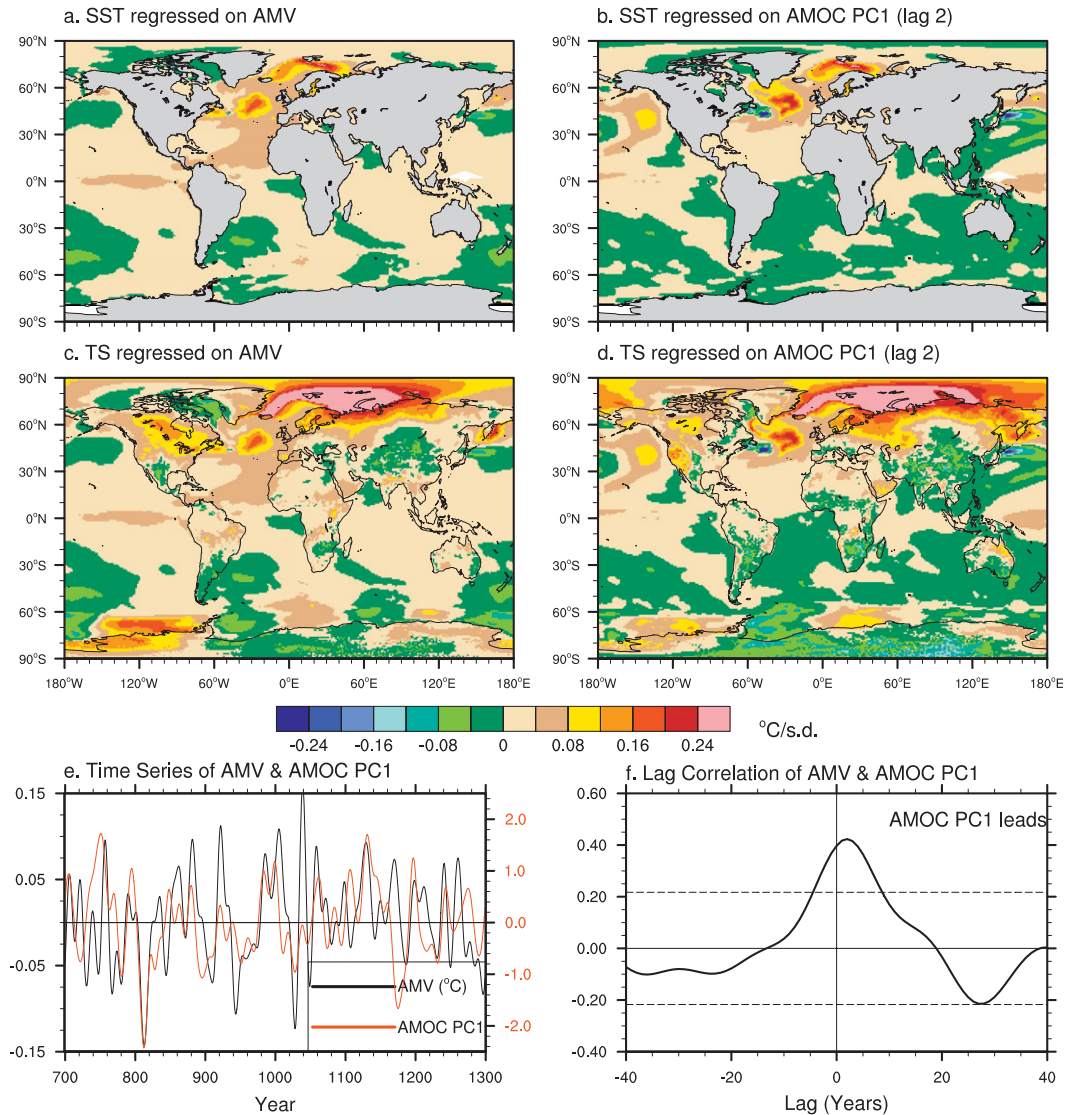
FIG. 5. Simultaneous regressions of the (a) SST and (c) surface temperature, TS, time series onto the normalized AMV index; regressions of the (b) SST and (d) TS time series onto the AMOC PC1 time series when the latter leads by 2 yr; (e) AMV index (black, left axis in °C) and AMOC PC1 (red, right axis) time series; and (f) AMOC PC1 time series correlation with the AMV index. AMOC PC1 leads for positive lags. The dashed lines show the 95% confidence level. In (a)–(d), the contour interval is 0.04°C per index standard deviation. A 15-yr low-pass Lanczos filter is used in all time series.

oceanic heat gain between 43° and 53°N—as indicated by the positive NHT slope—is a common feature of many other CCSM simulations and is associated with the atmospheric model acting to damp the large, cold SST bias, resulting from the incorrect path of the North Atlantic Current (Danabasoglu et al. 2012). The regression of the NHT time series with those of the AMOC PC1 shows enhanced NHT associated with larger AMOC transport (Fig. 4b). The largest magnitudes with 0.025 PW occur for simultaneous regressions. Using a typical AMOC PC1 amplitude of 2, the amplitude of NHT variability is about 0.05 PW, corresponding to only about 4% of the maximum

transport. Thus, this variability is 2.5 times smaller than in CCSM3 regime I (Danabasoglu 2008).

b. Surface temperatures and AMOC

To characterize the model's AMV, we calculate an AMV index following a similar method to that of Sutton and Hodson (2005). The index uses annual-mean SSTs averaged within the North Atlantic domain defined by 0°–60°N and 75°–7.5°W. It is detrended and a 15-yr low-pass Lanczos filter is applied. The resulting AMV index time series (black line in Fig. 5e) varies roughly between −0.15° and 0.15°C. Figure 5a gives the associated global

SST pattern obtained as the simultaneous regression of the SST time series onto the AMV index. The North Atlantic exhibits positive anomalies with the largest magnitudes located at about 30°W, 50°N (>0.16°C) and between Spitsbergen and Scandinavia (>0.24°C). These sites coincide with the subpolar–subtropical gyre boundary and sea ice edge, respectively. While weaker cold anomalies (≈0.04°C) occur mostly in the Southern Hemisphere, the largest cold anomaly (>0.08°C) occurs again at the subpolar–subtropical gyre boundary but this time in the western North Pacific Ocean. The SST pattern depicted in Fig. 5a is in broad agreement with the observations (e.g., Sutton and Hodson 2005), particularly in the Atlantic Ocean both showing a roughly interhemispheric pattern with large warm anomalies in the North Atlantic. There are differences, however, in the locations of the largest positive anomalies. Some other differences include cold versus warm anomalies in the North Pacific and weak warm versus weak cold anomalies in the equatorial Pacific in the model versus observations, respectively.

It is of interest to see if the SST pattern associated with the AMV has any similarities to the SST pattern associated with the AMOC variability. We obtain the latter pattern by regressing the SST time series onto the AMOC PC1 time series (Fig. 5b). Because the maximum correlations between the AMOC PC1 and AMV time series are attained when the former leads the latter by 2 yr (Fig. 5f), the regression shown is for when the AMOC PC1 leads the SST time series by 2 yr. For consistency, the same 15-yr low-pass Lanczos filter is used. We show the resulting low-frequency AMOC PC1 time series in Fig. 5e (red line). Comparison of Figs. 5a and 5b reveals that the two SST patterns are broadly similar with warm anomalies in the North Atlantic—including the locations of their maxima, weak cold anomalies mostly in the Southern Hemisphere, and cold anomalies in the North Pacific. However, the Southern Hemisphere and North Pacific cold anomalies are more extensive in Fig. 5b and there is a cold anomaly centered at about 45°W, 45°N in Fig. 5b which is largely missing in Fig. 5a.

Figures 5c and 5d present the corresponding AMV index and AMOC PC1 time series regressions with the atmospheric surface temperature (TS) time series. TS is equivalent to SST over the ice-free oceans. As in the SST regressions, TS patterns for both indices are broadly similar, with both showing substantial warming over sea ice in the eastern Arctic and northern North Atlantic, general warming over North America, cooling over central Asia and in broad regions in Antarctica and warming to the west of the Antarctic Peninsula. These regression patterns suggest influences of global teleconnections associated with the AMV and AMOC PC1 time series. The simultaneous regressions of precipitation on to the AMV

index (not shown) reveal a northward shift of precipitation in the tropical Atlantic—associated with a northward displacement of the intertropical convergence zone—and enhanced precipitation over the Sahel region, both consistent with observations and previous model studies (e.g., Sutton and Hodson 2005; Knight et al. 2006; Zhang and Delworth 2006). Over North America and India, however, the precipitation anomalies of both signs are present.

As indicated above, the correlation function between the AMV index and the AMOC PC1 time series indicate that the correlation is the largest (0.42) when the AMOC PC1 leads the AMV index by 2 yr (Fig. 5f). In a recent study, Medhaug and Furevik (2011) document that all 10 coupled models they considered for analysis have their largest correlations between AMOC and AMV time series when the former leads the latter as in CCSM4. However, the lead times vary between 1–7 yr (seven models) and 18–28 yr (3 models). Thus, the present model, along with its predecessor also showing a 2-yr lead, is among the models with relatively short lead times. A detailed investigation of these model differences, however, is beyond the scope of this work. The low-frequency AMV index time series (Fig. 5e) has a spectrum that shows a broad, statistically significant band for the 15–50-yr range (not shown). This range overlays with the lower end of the observed AMV periodicity, but the latter record is rather short.

c. AMOC and Nordic Sea overflows

Dense waters formed in the Nordic Sea flow through DS and FBC as gravity current overflows. These waters together with the LS deep convection supply the NADW. The combined DS and FBC parameterized product water transport (PT) in CCSM4 is about 5.2 Sv in the time mean, lower than the observational range of 6.4–9.4 Sv, primarily due to low entrainment (see Danabasoglu et al. 2012 for further details). We present the PT time series correlation with those of the AMOC PC1 in Fig. 6a, clearly showing that the strengthening of AMOC as depicted by the AMOC PC1 leads the increased PT by 6–8 yr. To show the effects of the Nordic Sea overflows on AMOC, the AMOC time series regressions with those of PT are given in Fig. 6b when PT leads by 2 yr. This time represents approximately the largest correlations between these time series for any PT lead times (not shown). The figure indicates reduced AMOC transports between 40° and 60°N above 2500-m depth associated with stronger PT, by as much as −0.35 Sv per PT unit variance. In contrast, the positive correlations north of 60°N above 2000-m depth and between about 25°–50°N below 3000-m depth are signatures of enhanced overturning circulation with larger PT. The latter is associated with the deeper NADW transport, resulting from the overflow parameterization. These findings are very similar to those of Yeager and
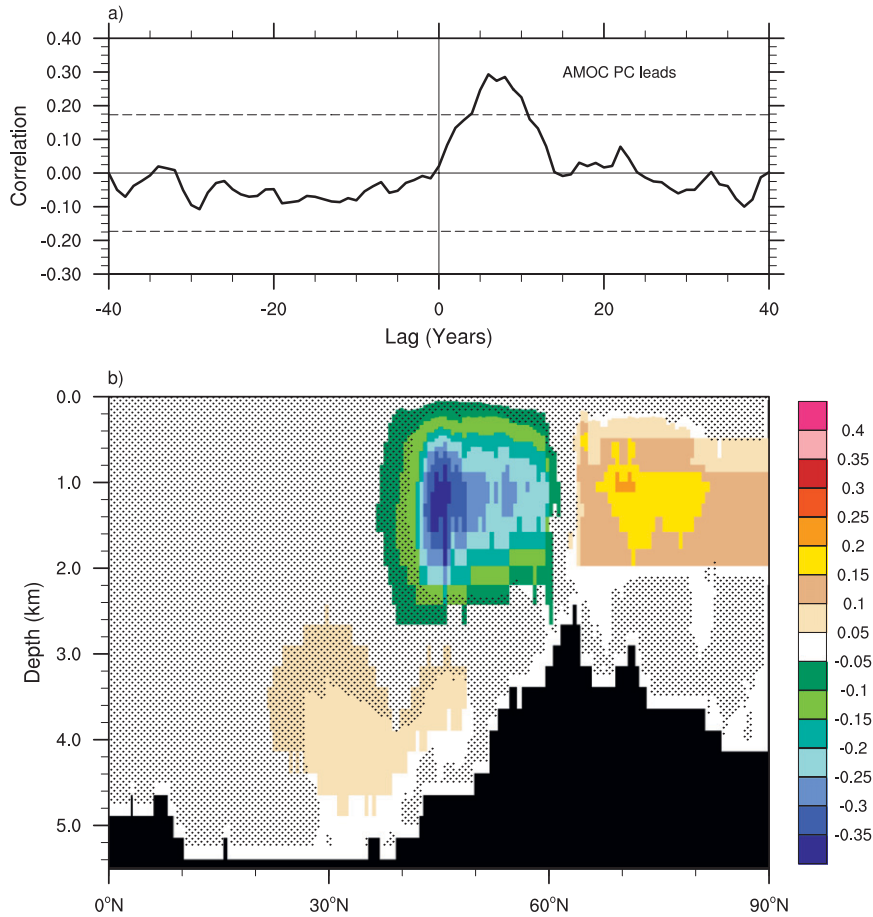
FIG. 6. (a) AMOC PC1 time series correlation with the combined Denmark Strait and Faroe Bank Channel overflows product water transport (PT) time series. The dashed lines show the 95% confidence level. AMOC PC1 leads for positive lags. (b) AMOC time series regression with the PT time series when the PT leads by 2 yr. The regression is in Sv per PT unit variance. No stippling denotes confidence above the 95% level.

Danabasoglu (2012) in which the reduced AMOC in the upper ocean following larger PT is associated with enhanced LS stratification and, hence, reduced LS convection. The LS stratification is maintained by the overflow waters.

We next focus on some relevant aspects of the overflow physics to understand the relationships between AMOC and PT time series described above. The overflow source transport is driven by the density difference between the source waters on the Nordic Sea side and the interior waters on the Atlantic side, defined by the source reduced gravity as $g'_{src} = g(\rho_{src} - \rho_{int})/\rho_0$. Here, g is the gravitational acceleration and ρ_0 is a constant reference density. Also, ρ_{src} and ρ_{int} represent the source and interior densities, respectively, both calculated at the sill depth (=483 and 787 m for DS and FBC, respectively). Similarly, the entrainment transport is driven by the entrainment reduced gravity given by $g'_{ent} = g(\rho^e_{src} - \rho_{ent})/\rho_0$,

where ρ^e_{src} and ρ_{ent} are the source and entrainment densities calculated at the entrainment depth (=879 and 985 m for DS and FBC, respectively). There is nonzero source transport only if $g'_{src} > 0$. For entrainment to exist, $g'_{ent} > 0$ must also be satisfied. The densities are obtained using average potential temperatures and salinities near the sill and entrainment depths as detailed in Danabasoglu et al. (2010). The product water properties are determined based on volume and tracer conservations.

With this brief background, we now present the source, interior, entrainment, and product water potential temperature, salinity, and ρ time series correlations with those of AMOC PC1 in Fig. 7. The figure also includes the AMOC PC1 time series correlations with g'_{src} and g'_{ent} time series. We show only the DS properties as the corresponding FBC properties produce similar results. Although some correlations remain below the 95% confidence level, the largest positive potential temperature
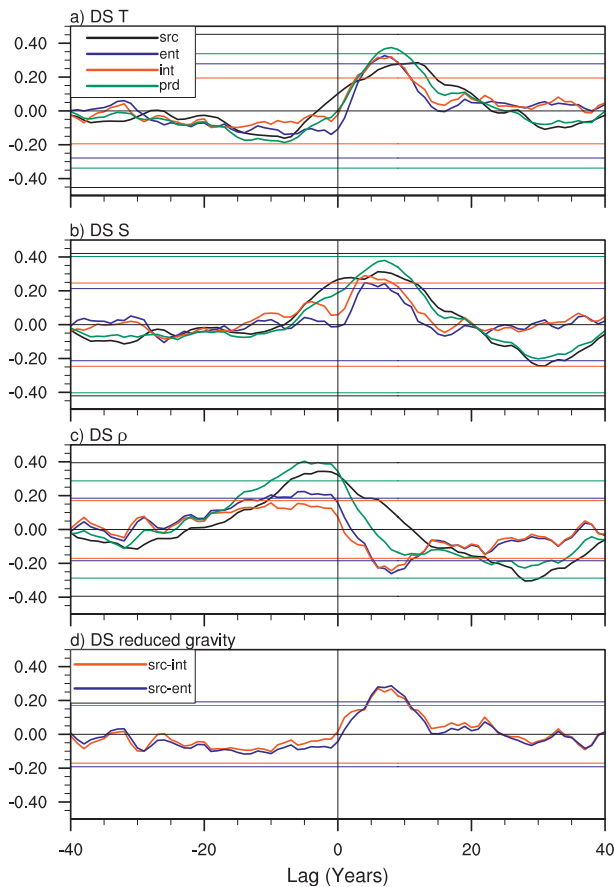
FIG. 7. Denmark Strait (DS) source (src), entrainment (ent), interior (int), and product (prd) water (a) potential temperature, (b) salinity, and (c) density time series correlations with the AMOC PC1 time series. (d) AMOC PC1 time series correlations with those of the src–int and src–ent reduced gravity (g'_{src} and g'_{ent}, respectively) time series described in the text. The thin color lines represent the 95% confidence levels for the respective variables with the same colors. AMOC PC1 leads for positive lags. In (c), the densities are referenced to the DS sill depth of 483 m. In (d), g'_{src} and g'_{ent} are referenced to 483 m and the DS entrainment depth of 879 m, respectively.

and salinity correlations occur roughly 4–10 yr after a strong AMOC, indicating transport of warm and salty anomalies into the northern North Atlantic with increased AMOC. We note that both the sill and entrainment depths given above are primarily within the depth range of the upper, that is, northward flowing, branch of AMOC. Prior to an AMOC maximum, while there are mostly negative potential temperature correlations, those for salinity remain largely positive between lag −10 and lag 0. The resulting ρ correlations indicate that the largest positive correlations occur roughly 1–7 yr prior to an AMOC maximum. After lag 0, all positive correlations diminish rapidly, with ρ_{int} and ρ_{ent} having their most negative correlations between lag +5 and lag +10. As discussed above,

the overflows are driven by g'_{src} and g'_{ent}, rather than the large positive ρ_{src} that peaks a few years before an AMOC maximum. Figure 7d clearly shows that both g'_{src} and g'_{ent} attain their maxima 6–8 yr after an AMOC maximum as represented by the AMOC EOF1, consistent with Fig. 6a. We also note that the densest product waters occur between lag −5 and lag −1 as seen in the corresponding regression plots (not shown), and thus they do not coincide with the largest PT, that is, the densest product waters do not necessarily imply increased PT.

In contrast with a recent study by Hawkins and Sutton (2008) where they find that increased DS overflow transport leads enhanced AMOC transport by 5–8 yr in the third climate configuration of the Met Office Unified Model (HadCM3), our findings indicate that increased overflow transports follow larger AMOC transports by 6–8 yr in CCSM4. Likely candidates for this major difference between these two models include parameterized representation versus explicit representation via artificially deepened topography in DS overflow and differences in deep convection regions and their variability. In CCSM4, increased PT appears to be a precursor to lower AMOC maximum transports together with some enhancement at depth, by about 1–2 yr.

d. Variability in the Labrador Sea region

Because increased overflow transports do not lead to an enhanced AMOC, we subsequently consider the DWF variability in the model to investigate what events proceed a high AMOC transport. For this purpose, we use March-mean boundary layer depth (BLD) distributions, as the BLD reaches its maximum in March. BLD is determined by the K-profile parameterization vertical mixing scheme (Large et al. 1994) as the shallowest depth at which a bulk Richardson number exceeds a specified critical Richardson number for the first time. In comparison with observational estimates, CCSM4 provides a much improved representation of the deep convection sites in LS—with maximum March-mean BLDs (1300–1400 m) occurring in the center of LS—than in CCSM3 (Danabasoglu et al. 2012). The BLD EOF1 and EOF2 account for 41% and 12% of the total variance, respectively. Their spatial patterns (not shown) are very similar to those of CCSM3: a monopole structure for EOF1 and a north–south dipole structure for EOF2 (see Danabasoglu 2008; Kwon and Frankignoul 2012). Both patterns are located primarily in LS, just south of Cape Farewell.

For analysis purposes, we define a LS DWF site bounded by 50°–60°N, 55°–35°W, and extending from surface to 203-m depth (indicated in Fig. 9) where the BLD variability is the largest. Figure 8a presents the AMOC PC1 time series correlations with the BLD and upper-ocean density (ρ_{uo}) index time series. Here, these indices are
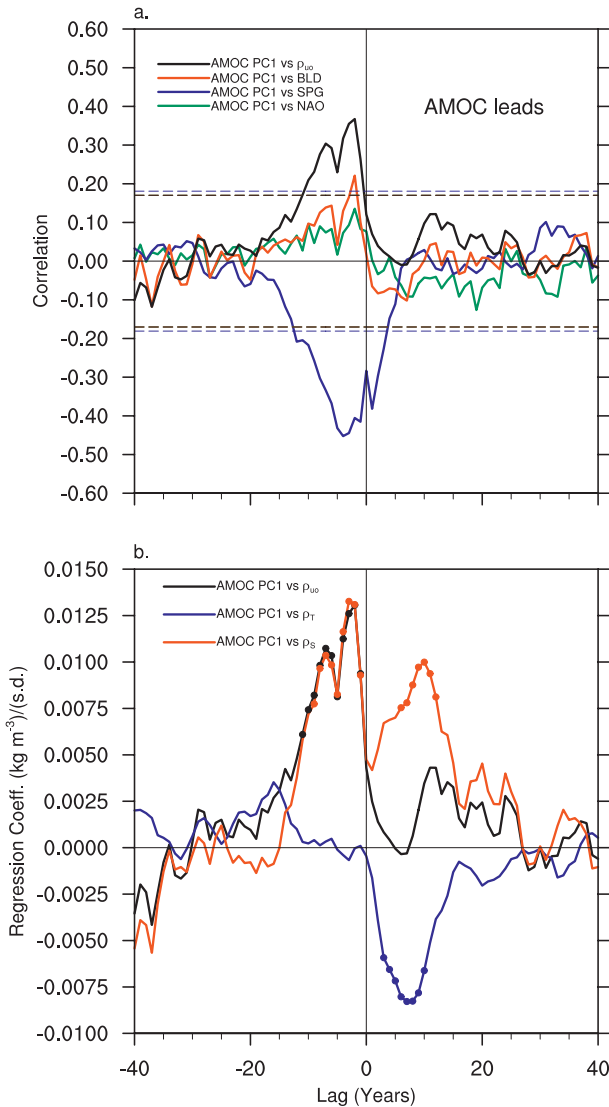
FIG. 8. (a) AMOC PC1 time series correlations with those of the upper-ocean density (ρ_{uo}), March-mean boundary layer depth (BLD), subpolar gyre index (SPG), and the NAO index. ρ_{uo}, BLD, and SPG represent averages within the LS box region identified in Fig. 9. Sea level pressure EOF PC1 is used for NAO. The 95% confidence levels are shown by the black dash line for ρ_{uo}, BLD, and NAO, and by the dark blue dash line for SPG. (b) ρ_{uo} time series regressions on to the AMOC PC1 time series within the LS box. The black line is for the total density. The temperature, ρ_T, and salinity, ρ_S, contributions to the total density are given by the blue and red lines, respectively. The regressions are in kg m^{-3} per index unit variance. The dots indicate the lags at which the corresponding correlations (not shown) have >95% confidence levels. AMOC PC1 leads for positive lags in both panels.

calculated as area and volume averages for BLD and ρ_{uo}, respectively, within this LS region. Starting at about lag −20, positive ρ_{uo} anomalies increase, getting statistically significant by lag −10. The maximum correlation between ρ_{uo} and AMOC is achieved when ρ_{uo} leads an

AMOC maximum by 2 yr. BLD correlation with AMOC follows closely that of ρ_{uo} with the deepest BLD anomalies again occurring 2 years prior to an AMOC maximum, consistent with the positive ρ_{uo} anomalies. We include the AMOC PC1 time series correlation with a subpolar gyre (SPG) index time series in Fig. 8a. Although the SPG index is calculated as the area-averaged barotropic (depth integrated) streamfunction within the analysis region, that is, relatively local, we believe that it represents a broader view of the entire SPG changes because the barotropic streamfunction regressions on to the AMOC PC1 time series (not shown) are generally consistent with Fig. 8a. The negative correlations indicate strengthening of the counterclockwise (cyclonic) SPG circulation. The largest SPG anomaly is obtained at lag −4, corresponding to a stronger and expanded SPG circulation in the western North Atlantic. Thereafter, correlations get weaker indicating slowing down of the SPG. There are accompanying warm and salty anomalies in the upper ocean (0–203 m average) in the eastern SPG, suggesting a contraction of the gyre after AMOC and BLD maxima. These features appear to be inconsistent with some recent observational studies (e.g., Hatun et al. 2005; Bersch et al. 2007), which find warm and salty anomalies in the upper ocean and a contracting SPG following reductions in the Labrador Seawater formation and in AMOC. The correlation of the SPG and ρ_{uo} (not shown) reveals that the enhanced SPG circulation lags the positive ρ_{uo} anomalies with the largest negative correlations occurring when ρ_{uo} leads by about 2 yr. We note that there is a small peak in the correlations between ρ_{uo} or BLD and AMOC PC1 when the former fields lead the latter by about 6 yr, corresponding to this 2-yr lag between ρ_{uo} or BLD and SPG. This relationship suggests a role for geostrophic adjustment (e.g., Delworth et al. 1993).

The AMOC PC1 time series correlations with the NAO time series is also shown in Fig. 8a. The NAO is defined as the wintertime (December–March) sea level pressure EOF1, and it shows a stronger-than-normal subtropical high pressure center in its positive phase (NAO+). This correlation remains below statistical significance at all lags. Nevertheless, there is a peak when NAO+ leads AMOC by 2 yr as in ρ_{uo} and BLD. The correlation of AMOC PC1 and the east Atlantic Pattern (EAP; wintertime sea level pressure EOF2) is similarly low at all lags. These suggest weak direct impacts of NAO and EAP on AMOC and vice versa. However, BLD and ρ_{uo} time series regressions on to the NAO time series (not shown) disclose positive BLD and ρ_{uo} anomalies that are statistically significant at lag 0 with correlation coefficients of 0.58 and 0.45, respectively. Furthermore, AMOC time series regressions on to those of the NAO show statistically significant

positive AMOC anomalies between about 35°–60°N and above 2000-m depth when the NAO leads by 2 yr. Conversely, the sea level pressure regressions on to the AMOC PC1 time series produce NAO+-like patterns starting at about lag −12 (AMOC lagging) and continuing through lag 0, but these NAO patterns remain below statistical significance.

The analysis presented in Fig. 8a suggests a driving role for the changes in model's DWF site in the LS region as positive ρ_{uo} anomalies lead to deeper BLDs, both leading a maximum in AMOC PC1 by 2 yr. While this time scale is the same as in regime II of CCSM3, it is shorter than in CCSM3 regime I, which exhibited a 4–5-yr lead for BLD and ρ_{uo} changes. It is also interesting to note that the ρ_{uo}, BLD, and SPG correlations diminish quite quickly for positive lags, implying weak AMOC influence on these fields.

Regression of the BLD time series onto the AMOC PC1 time series for BLD leading by 2 yr reveals essentially the same spatial pattern as the BLD EOF1 (Fig. 9). In contrast with CCSM3, however, the location of the maximum regression is not collocated with the maximum March-mean BLD site (see Danabasoglu et al. 2012). Instead, the regression plot shows large variability coincident with strong mean BLD gradients, suggesting southward expansion/contraction of the primary deep convection region as in Yeager and Danabasoglu (2012). We present the regression of ρ_{uo} time series onto those of the AMOC PC1 in the same figure. It is for ρ_{uo} leading AMOC PC1 also by 2 yr as this is when the maximum correlations occur between these two fields (Fig. 8a). Positive ρ_{uo} anomalies occur in a broad region extending southward and eastward from LS to about 43°N and 20°W. The maximum positive ρ_{uo} anomalies do not coincide with the maximum BLD anomaly location. This is again different than in CCSM3 where the two anomalies were largely collocated. The largest positive ρ_{uo} anomalies located near 43°N, 50°W are associated with the cold anomalies that persist in this region from lag −10 (AMOC PC1 lagging) to lag +10 (AMOC PC1 leading) (see Fig. 5b). North of 48°N and north of Iceland, the density anomalies primarily reflect positive salinity anomalies. The broad negative anomaly region west of North America is due to a warm anomaly that peaks at this lag in this region. This warm anomaly appears to be forced by the atmosphere as the surface heat flux regressions both on to the NAO index time series at lag0 and on to those of the AMOC PC1 at lag −2 (AMOC lagging) show positive heat flux anomalies. Increasing AMOC transport may also contribute to this warming.

Kwon and Frankignoul (2012) emphasized the role of advection of density anomalies from the eastern subpolar gyre to the LS DWF site in long persistence of red noise–
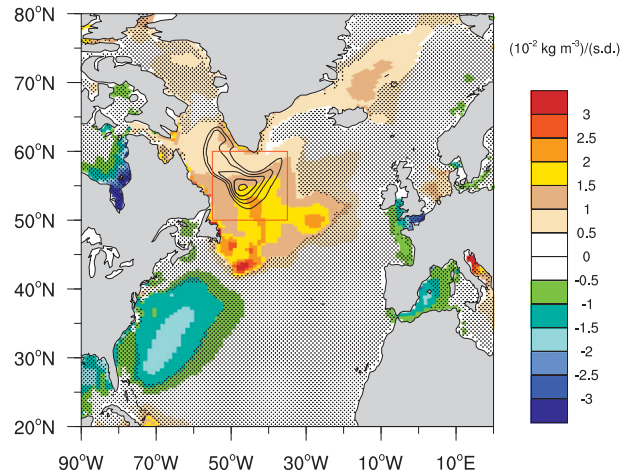

FIG. 9. The upper-ocean (0–203-m average) density (color) and march-mean boundary layer depth (black contours) time series regressions onto the AMOC PC1 time series when the AMOC PC1 lags by 2 yr. The contour interval is 25 m per AMOC PC1 unit variance for the boundary layer depth regression. No stippling denotes confidence above the 95% level. The boxed region indicates the analysis domain for the Labrador Sea convection site density.

like regime II in CCSM3. There, the density anomalies found near the British Isles were advected into the DWF site in 5–7 yr. In CCSM4, ρ_{uo} anomalies with the opposite sign to those in the LS DWF site are first found in the western subtropical gyre and later expand into the eastern half of the subpolar gyre (not shown) more similar to the regime I of CCSM3. However, the anomalies become damped significantly as they are advected into the DWF site in the subsequent years. Therefore, the mechanism suggested by Kwon and Frankignoul (2012) for either regime of CCSM3 does not seem to exist in CCSM4.

Figure 8b presents the AMOC PC1 regressions with ρ_{uo} for this DWF location along with the individual temperature, ρ_T, and salinity, ρ_S, contributions. The regression coefficients are volume averaged. The densest waters start to form roughly at about lag −20 and the maximum positive ρ_{uo} anomaly is obtained just 2 yr prior to an AMOC maximum. This increase in ρ_{uo} is entirely due to ρ_S, as ρ_T contribution remains near zero. In contrast, following an AMOC maximum, warm anomalies start to form with their maximum occurring at about lag +8, partly compensating the persistent salty anomalies. This compensation of ρ_S anomalies by those of ρ_T, that is, spicy behavior, after an AMOC maximum damps the positive ρ_{uo} anomalies. Indeed, ρ_{uo} anomaly weakens to near zero values within 5 yr. These ρ_T and ρ_S phase relationships both before and after an AMOC maximum are in stark contrast with what is observed in CCSM3 regimes where ρ_T and ρ_S contributed almost equally to ρ_{uo} prior to an AMOC maximum, and afterward no significant compensating ρ_T and ρ_S contributions to ρ_{uo} was seen.

e. Heat and freshwater budgets at the LS DWF site

To document the creation of the ρ_{uo} anomalies that are associated with deeper BLDs and larger AMOC transports, we perform heat and freshwater budget analysis for the LS DWF site denoted by the boxed region in Fig. 9 (see the appendix for details). The budget terms are presented as regressions with the AMOC PC1 time series for heat and freshwater fluxes in Figs. 10 and 11, respectively. The positive (negative) fluxes indicate heat and freshwater input (loss) to (from) the budget volume. As indicated in the appendix, an important new feature of the current analysis is the explicit calculations of the parameterized mesoscale (ADV_{MESO}) and submesoscale ($ADV_{SUBMESO}$) advective flux contributions. This is in contrast with CCSM3 where the mesoscale velocities were not available and no submesoscale mixed layer eddy parameterization was used. In both figures, panels a, b, and c have the same respective scales to display all the individual horizontal and vertical advective fluxes, showing that the parameterized fluxes are comparable in magnitude to those due to the mean flow. Indeed, ADV_{MEAN} (mean flow advection), ADV_{MESO}, and $ADV_{SUBMESO}$ (Figs. 10d and 11d) have similar magnitude contributions to the budgets, stressing the importance of subgridscale parameterizations at this DWF site. As in CCSM3, generally, the budget analysis reveals significant cancellations among various terms, and contributions from all terms become important. For example, the mean advective freshwater flux from the southern boundary (S) is largely compensated by the mean advective flux from the eastern and northern boundaries ($E + N$) between lag -15 and lag $+10$ (Fig. 11a) or, alternatively, as more salt is coming in through $E + N$, more is going out through S. This is consistent with an enhanced SPG circulation as indicated in Fig. 8a (see also Fig. 12).

Prior to an AMOC maximum, starting at about lag -16, the total advective flux, that is, $ADV_{MEAN} + ADV_{MESO} + ADV_{SUBMESO}$, and the diffusive flux act to increase the upper-ocean temperature while the surface fluxes have an opposite effect (Fig. 10e). The latter peaks at about lag -2, coinciding with a positive NAO phase. Indeed, surface heat flux regressions on to the NAO time series reveal statistically significant negative heat flux anomalies at lag0 (not shown). Between lag -16 and lag 0, we calculate the total advective (ADV), diffusive (DIFF), and surface (SFLX) flux averaged contributions as $+0.74$, $+0.63$, and -1.32 W m^{-2}, respectively, resulting in a net (TOTAL) flux of only $+0.05$ W m^{-2}. This net positive flux anomaly acts to change an initially cold anomaly (with a peak at lag-16) to a smaller magnitude warm anomaly after about lag -5. However, the impact on ρ_{uo} is rather negligible as shown in Fig. 8b because density

variations are determined largely by salinity changes at cold temperatures. We further note that $ADV_{MEAN} = +0.36$, $ADV_{MESO} = +0.24$, and $ADV_{SUBMESO} = +0.14$ W m^{-2} between lag -16 and lag 0, indicating that the sum of the parameterized advective contributions is larger than ADV_{MEAN}. Thus, including DIFF, the parameterizations account for >1 W m^{-2} in this region.

The salinity anomalies that dominate ρ_{uo} prior to an AMOC maximum start to form at about lag -15, peaking at about lag -3 (Fig. 11e). Between these two lags, the averaged contributions from all components act to increase salinity with negative freshwater fluxes. Specifically, $ADV = -1.3 \times 10^{-7}$, $DIFF = -1.0 \times 10^{-7}$, and $SFLX = -0.9 \times 10^{-7}$ kg m^{-2} s^{-1}, producing a net freshwater loss of -3.2×10^{-7} kg m^{-2} s^{-1} over this period. This loss increases the volume-mean salinity of the LS DWF site by >0.017 psu by lag -3, leading to the positive ρ_{uo} anomaly. A further breakdown of the advective fluxes shows $ADV_{MEAN} = -0.93 \times 10^{-7}$, $ADV_{MESO} = -0.29 \times 10^{-7}$, and $ADV_{SUBMESO} = -0.05 \times 10^{-7}$ kg m^{-2} s^{-1}, with parameterized advective fluxes accounting for about 25% of the total advective contribution. Including DIFF, the parameterizations are responsible for over 1.3×10^{-7} kg m^{-2} s^{-1}, about 40% of TOTAL.

The above analysis shows that the parameterized advective fluxes contribute to increased positive salinity anomalies that eventually lead to increased BLD. This may be interpreted as counterintuitive because both the mesoscale and submesoscale parameterizations are designed to flatten isopycnals. To further explore, we show the 0–203-m-depth average horizontal velocity simultaneous regressions with the ρ_{uo} time series for the mean, mesoscale, and submesoscale velocities in Fig. 12. The mean velocity regression largely reflects circulation anomalies consistent with enhanced subpolar gyre circulation. On the other hand, the regressions for both parameterized velocities distinctly show convergent flow patterns whose centers are collocated with the deepest BLD anomalies. Thus, the parameterizations act to flatten isopycnals as expected (Gent et al. 1995). Furthermore, the associated heat and freshwater horizontal advective transports are spicy (i.e., largely density compensating), particularly between lag -10 and lag 0: while the heat fluxes show positive anomalies (Figs. 10b and 10c), the freshwater flux anomalies remain negative (Figs. 11b and 11c). Figure 10e shows that the surface heat flux anomalies more than counteract the warming due to ADV_{MESO} and $ADV_{SUBMESO}$. In contrast, the negative freshwater flux anomalies from all components survive, resulting in larger upper-ocean salinities and, hence, larger ρ_{uo}.

After an AMOC maximum, the temperature and salinity anomalies have opposing contributions to density,
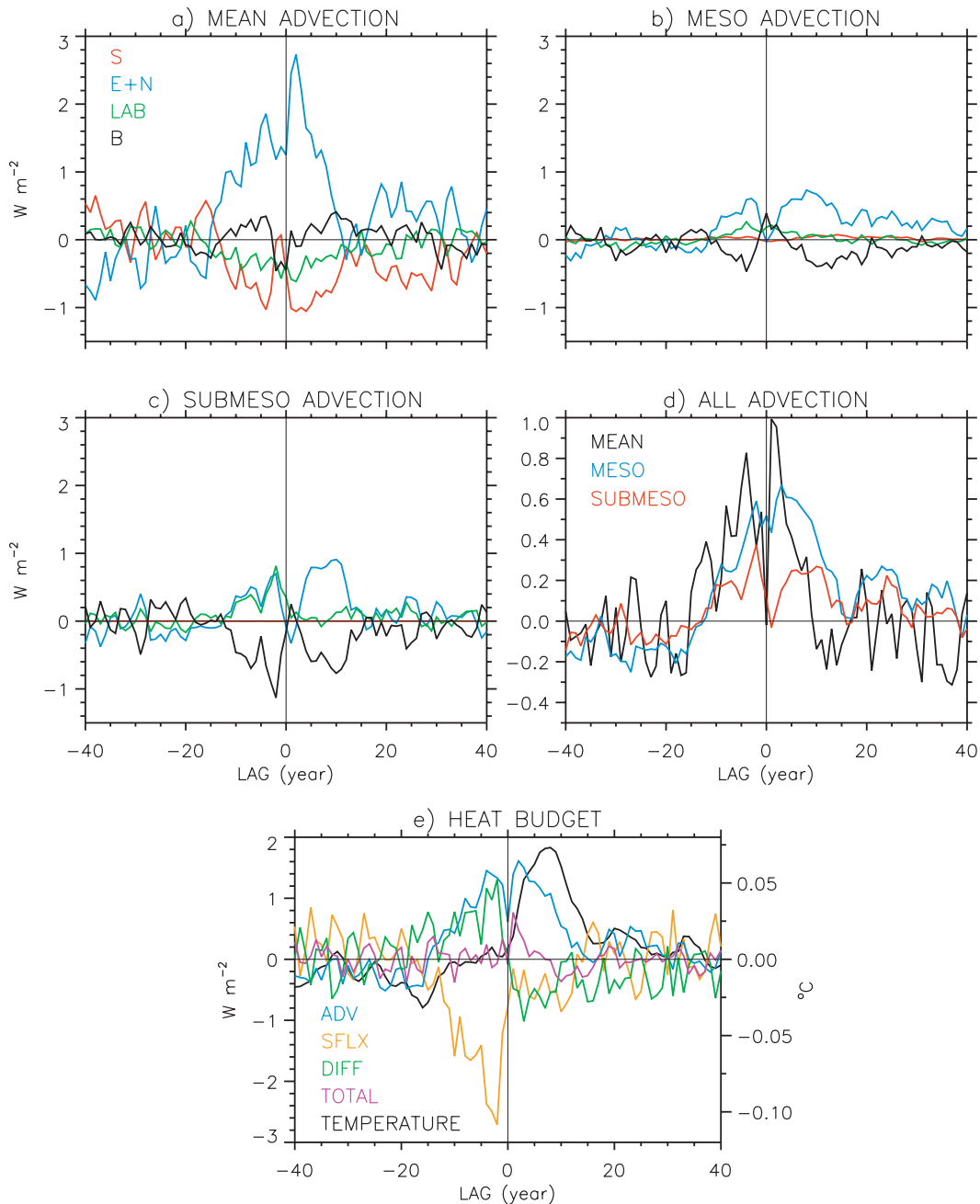
FIG. 10. Regressions of the heat budget terms with the AMOC PC1 time series for the LS convection site shown in Fig. 9. Horizontal advective contributions across the southern face (*S*), across the eastern and northern (segment east of Cape Farewell) faces (*E* + *N*), across the faces on the LS side (LAB), and vertical advective transport across the 203-m depth level (*B*) are shown for (a) resolved mean flow (MEAN), (b) parameterized mesoscale flow (MESO), and (c) parameterized submesoscale flow (SUBMESO). (d) The sums of all the advective transport contributions, that is, *S* + *E* + *N* + LAB + *B*, for MEAN, MESO, and SUBMESO. (e) The heat budget terms. Here, SFLX and DIFF represent total surface flux and horizontal and vertical diffusive fluxes, respectively. ADV is the sum of all advective fluxes, and TOTAL = SFLX + DIFF + ADV. In (e), TEMPERATURE is the volume-mean potential temperature within the budget region with its scale given on the right vertical axis. AMOC PC1 leads for positive lags.
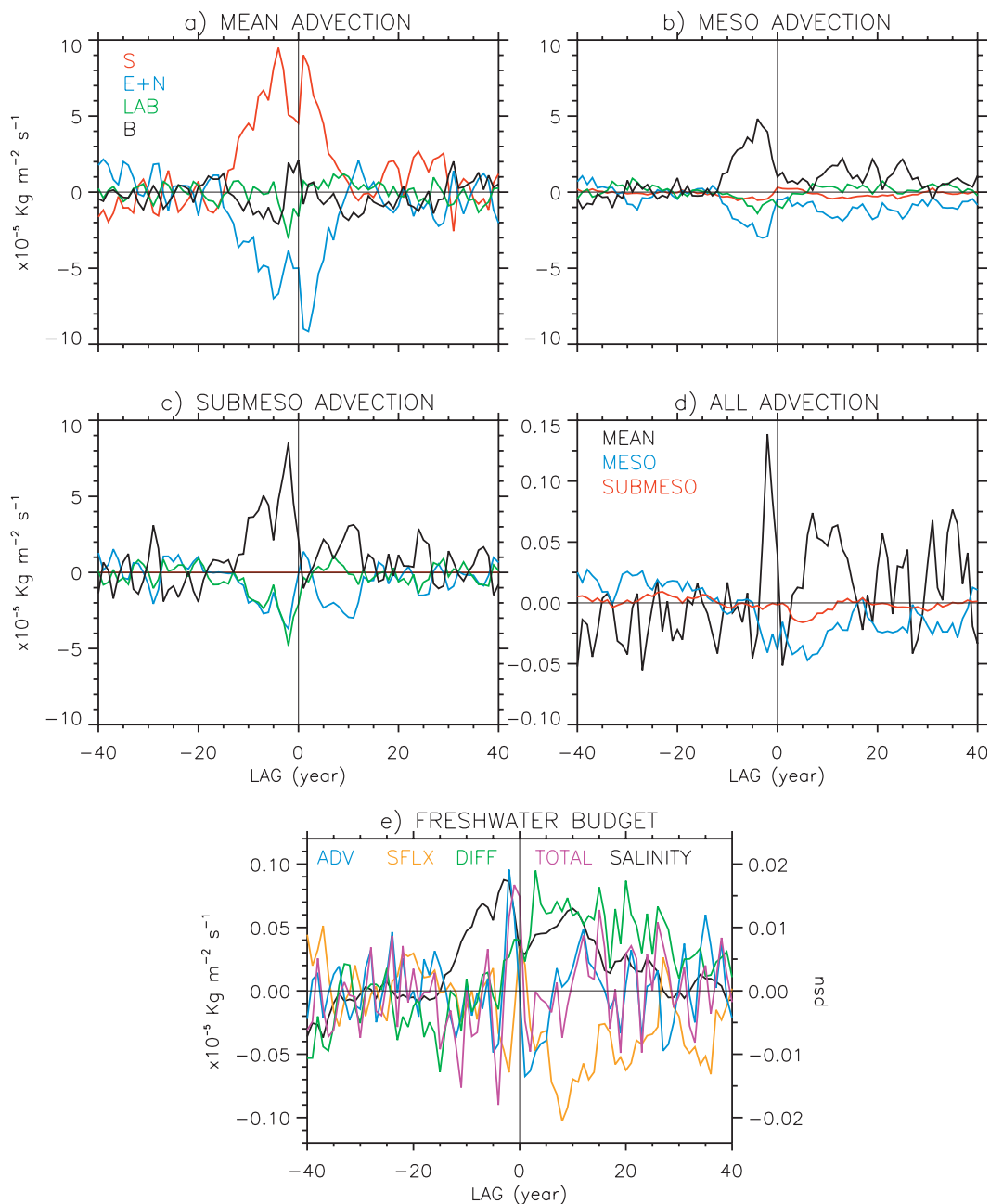
FIG. 11. As in Fig. 10, but for the freshwater budget. In (e), SALINITY is the volume-mean salinity within the budget region with its scale given on the right vertical axis. The positive (negative) fluxes indicate freshwater input (loss) to (from) the budget region.

and remain so beyond lag +15 (Figs. 10e and 11e). The advective terms clearly lead to the warming tendency seen up to lag +8. This results from advective fluxes from $E + N$, initially due to the mean advection then followed by both mesoscale and submesoscale fluxes. Here, the warm anomalies appear to be generated at the subtropical–subpolar gyre boundary east of 40°W at lag 0 and get advected by the subpolar gyre into the LS

DWF site (not shown). The positive salinity anomalies are largely maintained by the negative surface freshwater fluxes. However, there are additional significant contributions from both mesoscale and submesoscale advective fluxes, both counteracting the freshening tendency of the mean advection till lag +7. We note that the enhanced S and $E + N$ mean advective fluxes spanning lag −15 to lag +10 roughly coincide with
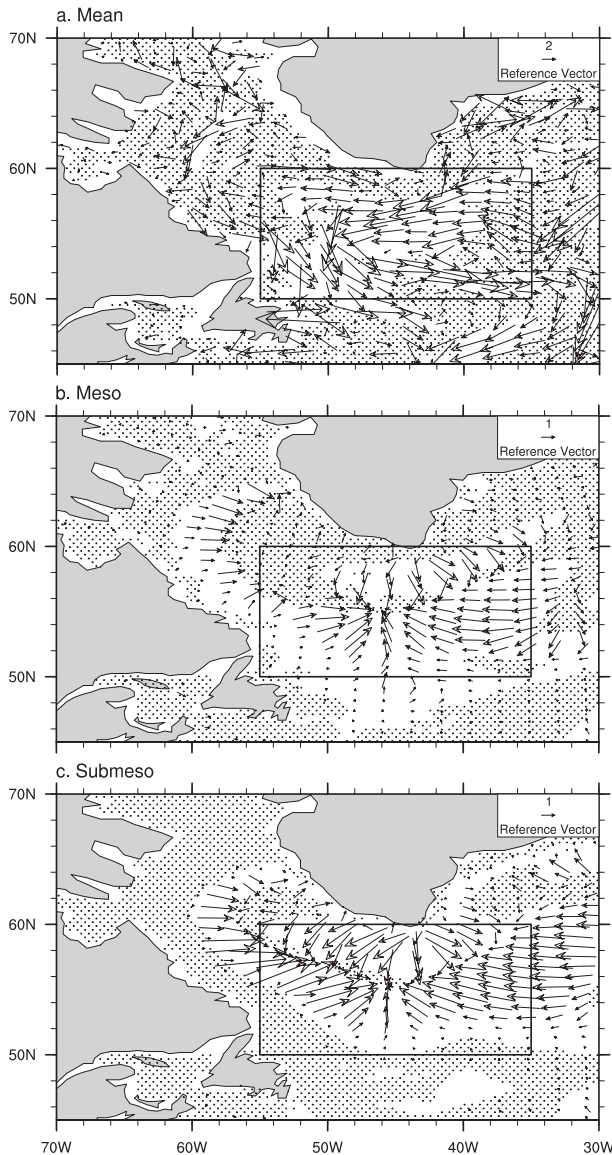
FIG. 12. Simultaneous regressions of the ρ_{uo} time series with the time series of the 0–203-m-depth-average horizontal velocities for (a) resolved mean, (b) parameterized mesoscale, and (c) parameterized submesoscale flows for the LS convection site. No stippling denotes confidence above the 95% level. The boxed area indicates the budget analysis region. The regressions are in (cm s^{-1})/(Kg m^{-3}).

stronger subpolar gyre circulation that occurs between about lag -10 and lag $+5$ (Fig. 8a).

4. Summary and conclusions

We have investigated the AMOC3 variability in the new CCSM4 preindustrial control simulation that uses nominal 1° horizontal resolution in its component models. AMOC in CCSM4, as represented by either its maximum transport or PC1 time series, clearly shows

some significant differences from CCSM3. Specifically, i) CCSM4 does not exhibit any distinct oscillatory behavior as in regime I of CCSM3; ii) the CCSM4 AMOC variability is much reduced—to about 12%–40% of the AMOC variance in CCSM3; and iii) CCSM4 AMOC shows low frequency, strongly damped variability with a broad, statistically significant band for the 50–200-yr range, in contrast with particularly regime I of CCSM3 where a much shorter, multidecadal peak of 21 yr existed.

In CCSM4, the NADW cell is slightly stronger and penetrates deeper than in CCSM3. The latter is due to the overflow parameterization. The AMOC EOF1 and EOF2 spatial patterns remain very similar between CCSM3 and CCSM4. In particular, EOF1 has a single-cell pattern, covering the entire Atlantic Basin south of 60°N in both models. This indicates that the NADW cell gets stronger and penetrates deeper in its positive phase. The CCSM4 mean Atlantic NHT is mostly within the range of implied transport estimates, but remains lower than the estimate based on the RAPID data. The largest positive NHT anomalies occur together with larger AMOC. However, as in AMOC, the CCSM4 NHT variability is also smaller than in CCSM3. Positive AMOC anomalies lead the hemispheric SST changes by 2 yr with generally warmer anomalies in the Northern Hemisphere and weaker cold anomalies in the Southern Hemisphere. This CCSM4 AMV pattern appears to be more realistic than in CCSM3, showing broad agreement with observations, particularly in the Atlantic Ocean. CCSM3 had a similar 2–3-yr lead of an AMOC maximum over the subsequent SST anomalies.

We find that an increase in the Nordic Sea overflow transports does not lead to an enhanced AMOC transport in CCSM4. Indeed, as in CCSM3, the AMOC variability is strongly associated with the variability at the LS DWF site. Figure 13 presents a schematic representation of sequence of anomalies with respect to an AMOC maximum (at lag0), indicating that the positive ρ_{uo} anomalies and the resulting deep BLD lead to increased AMOC. Both ρ_{uo} and BLD attain their maximum positive anomalies just 2 yr prior to an AMOC maximum. Here, ρ_{uo} anomalies are entirely due to increased salinities. Associated with larger AMOC, warm anomalies develop with their maximum occurring at about lag $+8$. These warm anomalies partly compensate the persistent salty anomalies, producing $\rho_{uo} \approx 0$ at lag $+6$. Roughly coinciding with this, increases in both source and entrainment reduced gravities result in increased overflow transports, subsequently enhancing the LS stratification. We believe that this enhanced stratification along with $\rho_{uo} \approx 0$ leads to a weakening in upper-ocean AMOC in about 10 yr following an AMOC maximum.
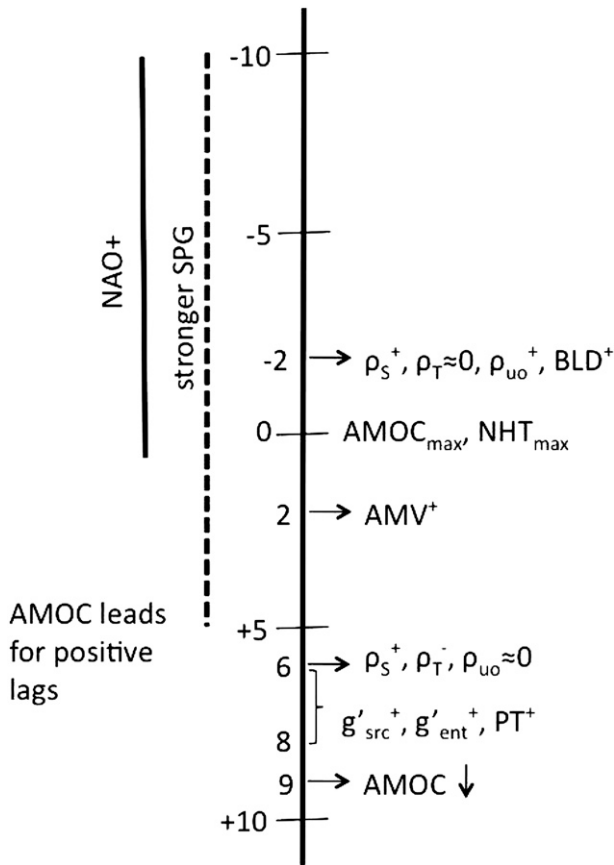
FIG. 13. Schematic of the sequence of some anomalies with respect to an AMOC maximum event at lag 0. The superscripts + and − refer to approximate peaks of positive and negative anomalies, respectively. AMOC leads for positive lags.

Our budget analysis for the LS DWF site shows that contributions from all terms, including those of the parameterized mesoscale and submesoscale eddies, are important in creating the positive ρ_{uo} anomalies that lead an AMOC maximum. For example, parameterized mesoscale eddy fluxes (both advective and diffusive) contribute substantially to the heat budget, while playing a role in the creation of salinity anomalies that dominate ρ_{uo}. Such dependence of AMOC variability on these parameterizations has important implications for both AMOC variability characteristics and search for a robust mechanism as they may depend on parameter choices and implementation details of these schemes in various ocean general circulation models. As indicated in Fig. 13, SPG circulation is stronger prior to an AMOC maximum. In addition, NAO tends to be in its positive phase during this period. The spectrum of the annual NAO time series (not shown) is overall white with only slightly enhanced variance in the interannual periods associated with ENSO. There are small peaks at the multidecadal and centennial bands, but they are not significant. Although NAO and AMOC PC1 time series correlations are below statistical significance, NAO is highly correlated (simultaneous) with the positive BLD and ρ_{uo} anomalies prior to an AMOC maximum. We speculate that persistent NAO+ may play a role in setting these positive anomalies through its impacts on surface fluxes and enhanced SPG circulation. Although there is certainly support for such a NAO role from studies concerning mid-1990s subpolar North Atlantic warming (e.g., Robson 2010; Robson et al. 2012; Yeager et al. 2012), it remains unclear for how long such NAO+ phase needs to persist. Finally, we believe that sea ice plays a passive role in this variability as the sea ice fraction regressions on to the AMOC PC1 do not reveal significant signals, particularly in the LS DWF region.

The positive density anomalies in the Nordic Sea overflow source regions peak 1–7 yr prior to an AMOC maximum. However, these larger source densities do not necessarily lead to increased overflow transports because the overflow physics is governed by the density differences between the source and interior as well as the source and entrainment regions. Furthermore, increased overflow transports do not lead to a higher AMOC either, but instead appear to be a precursor to lower AMOC transports through enhanced stratification in LS. This has major implications for decadal prediction studies involving AMOC, as positive density and higher overflow transport anomalies cannot necessarily be used as precursors for larger AMOC transports in the upper ocean. There is, however, enhanced AMOC at depth, 1–2 yr following increased overflow transports.

The present results related to mechanisms differ from our previous CCSM3 analysis in several important aspects. To list a few: both ρ_S and ρ_T contributed to the positive ρ_{uo} anomalies prior to an AMOC maximum in CCSM3, not just ρ_S as in CCSM4; the lead time for these ρ_{uo} anomalies was 5 yr in CCSM3 regime I instead of 2 yr in CCSM4; and a suggested, CCSM3 mechanism involving advection of density anomalies from the eastern subpolar gyre to the LS DWF site (Kwon and Frankignoul 2012) does not exist in CCSM4. Thus, the search for a robust mechanism still remains illusive. Nevertheless, there are some significant common features between CCSM3 and CCSM4. These include coupling of the LS DWF site and AMOC maximum variabilities, role of ρ_{uo} in driving these anomalies, existence of enhanced SPG circulation, and links with a (*persistent*) NAO+ phase.

An important outstanding issue is what sets the low-frequency time scale in CCSM4. Our efforts in search of this have not been successful because there are no apparent

trackable, propagating signals—either advective or wave mechanisms—into the LS DWF region on these long time scales. Emergence of a long NAO+ phase remains an attractive possibility for setting the ripe conditions for positive ρ_{uo} anomalies to form prior to an AMOC maximum, but again this does not provide a time scale.

Finally, for the CCSM3 regime I, Danabasoglu (2008) raised a possibility of the covariability between the decadal variability of the AMOC and the Pacific decadal variability (PDV) especially around 20-yr periodicity. In CCSM4, the PDV still exhibits strong variability around 15–20 yr centered around the Kuroshio–Oyashio Extension as in the previous versions of CCSM (Alexander et al. 2006; Kwon and Deser 2007; Deser et al. 2012), while AMOC no longer exhibits enhanced variance around 20 yr (Fig. 2). Lag regression of global SST and precipitation on AMOC suggest that only a weak correlation between the Pacific SST and AMOC exists through weak projection of the El Niño–Southern Oscillation on the NAO primarily in the interannual frequency (not shown).

APPENDIX

Heat and Freshwater Budget Details

The budget volume is defined by the boxed area in Fig. 9, extending from surface to 203-m depth. Our present analysis follows the same procedure described in Danabasoglu (2008) with one major exception: the parameterized mesoscale and submesoscale advective contributions are explicitly calculated. POP2 uses the Gent and McWilliams (1990) mesoscale eddy parameterization in its skew flux form (Griffies 1998). The mixed layer eddy, submesoscale mixing parameterization of Fox-Kemper et al. (2008) is cast as an overturning vector streamfunction. Consequently, the corresponding advective velocities for both parameterizations are calculated diagnostically at each model time step. The model equations are discretized on the B grid (Arakawa and Lamb 1977). Thus, while the resolved mean flow horizontal velocity components are located at the tracer grid cell corners, the grid–longitudinal and grid–latitudinal parameterized horizontal velocity components are obtained at the eastern and northern face centers of the tracer grid cells, respectively. All vertical velocities are located at the bottom centers of the tracer grid cells.

We write the model tracer equations as

$$\text{TEN} = -\text{ADV}_{\text{MEAN}} - \text{ADV}_{\text{MESO}} - \text{ADV}_{\text{SUBMESO}} + \text{SFLX} + \text{DIFF}, \tag{A1}$$

where ADV_{MEAN}, ADV_{MESO}, and $\text{ADV}_{\text{SUBMESO}}$ represent the advective fluxes due to the resolved mean flow, parameterized mesoscale flow, and parameterized submesoscale flow, respectively. Also, TEN is tendency, SFLX is the total surface flux, and DIFF represents the total parameterized horizontal, isopycnal, and vertical diffusive fluxes, including convection. All ADV fluxes are further divided into horizontal and vertical components as follows:

$$\text{ADV} = S + E + N + \text{LAB} + B. \tag{A2}$$

Here, S is the horizontal advective flux from the southern face, $E + N$ is the horizontal advective flux from the eastern and northern (segment east of Cape Fairwell) faces, LAB is the horizontal advective flux from the LS side, and finally, B is the vertical advective flux from the bottom, that is, 203-m depth. These advective fluxes are obtained based on the conservative form of the model equations, and hence, involve tracer times plane-normal velocity component multiplications. For example, to calculate components of S, we use v_{MEAN} Tr, v_{MESO} Tr, and v_{SUBMESO} Tr for the mean, mesoscale, and submesoscale advection. Here, v is the grid–latitudinal velocity component and Tr is a generic tracer. The quantities v_{MEAN} and Tr are averaged in the grid–longitudinal and grid–latitudinal directions, respectively, so that they are located at the center of the northern face of the tracer grid cells.

The positive (negative) fluxes indicate heat and freshwater input (loss) to (from) the budget region. Individual

budget terms are computed using monthly-mean data. We then create annual-mean, detrended time series for each component and regress these with the AMOC PC1 time series. TEN is evaluated based on the differences of two subsequent January-mean values and DIFF is obtained as a residual. Also, the temperature and salinity are in °C and psu, respectively. All fluxes with the exception of SFLX are normalized by the surface area of the analysis region so that all terms have the same units, that is, W m^{-2} and kg m^{-2} s^{-1} for heat and freshwater fluxes, respectively.

REFERENCES

Alexander, M., and Coauthors, 2006: Extratropical atmosphere–ocean variability in CCSM3. *J. Climate,* **19,** 2496–2525.

Arakawa, A., and V. R. Lamb, 1977: Computational design of the basic dynamical processes of the UCLA general circulation model. *Methods Comput. Phys.,* **17,** 174–265.

Bersch, M., I. Yashayaev, and K. P. Koltermann, 2007: Recent changes of the thermohaline circulation in the subpolar North Atlantic. *Ocean Dyn.,* **57,** 223–235, doi:10.1007/s10236-007-0104-7.

Branstator, G., and H. Teng, 2010: Two limits of initial-value decadal predictability in a CGCM. *J. Climate,* **23,** 6292–6311.

Bryan, F. O., G. Danabasoglu, N. Nakashiki, Y. Yoshida, D. H. Kim, J. Tsutsui, and S. C. Doney, 2006: Response of North Atlantic thermohaline circulation and ventilation to increasing carbon dioxide in CCSM3. *J. Climate,* **19,** 2382–2397.

Collins, W. D., and Coauthors, 2006: The Community Climate System Model, version 3 (CCSM3). *J. Climate,* **19,** 2122–2143.

Cunningham, S. A., and Coauthors, 2007: Temporal variability of the Atlantic meridional overturning circulation at 26.5°N. *Science,* **317,** 935–938, doi:10.1126/science.1141304.

Danabasoglu, G., 2008: On multidecadal variability of the Atlantic meridional overturning circulation in the Community Climate System Model version 3. *J. Climate,* **21,** 5524–5544.

——, and J. Marshall, 2007: Effects of vertical variations of thickness diffusivity in an ocean general circulation model. *Ocean Modell.,* **18,** 122–141, doi:10.1016/j.ocemod.2007.03.006.

——, R. Ferrari, and J. C. McWilliams, 2008: Sensitivity of an ocean general circulation model to a parameterization of near-surface eddy fluxes. *J. Climate,* **21,** 1192–1208.

——, W. G. Large, and B. P. Briegleb, 2010: Climate impacts of parameterized Nordic Sea overflows. *J. Geophys. Res.,* **115,** C11005, doi:10.1029/2010JC006243.

——, S. C. Bates, B. P. Briegleb, S. R. Jayne, M. Jochum, W. G. Large, S. Peacock, and S. G. Yeager, 2012: The CCSM4 ocean component. *J. Climate,* **25,** 1361–1389.

Delworth, T. L., and M. E. Mann, 2000: Observed and simulated multidecadal variability in the Northern Hemisphere. *Climate Dyn.,* **16,** 661–676.

——, S. Manabe, and R. J. Stouffer, 1993: Interdecadal variations of the thermohaline circulation in a coupled ocean-atmosphere model. *J. Climate,* **6,** 1993–2011.

Deser, C., and Coauthors, 2012: ENSO and Pacific decadal variability in Community Climate System Model version 4. *J. Climate,* **25,** 2622–2651.

Dong, B., and R. T. Sutton, 2005: Mechanism of interdecadal thermohaline circulation variability in a coupled ocean–atmosphere GCM. *J. Climate,* **18,** 1117–1135.

D'Orgeville, M., and W. R. Peltier, 2009: Implications of both statistical equilibrium and global warming simulations with CCSM3. Part II: On the multidecadal variability in the North Atlantic basin. *J. Climate,* **22,** 5298–5318.

Duchon, C. E., 1979: Lanczos filtering in one and two dimensions. *J. Appl. Meteor.,* **18,** 1016–1022.

Farneti, R., and G. K. Vallis, 2011: Mechanisms of interdecadal climate variability and the role of ocean-atmosphere coupling. *Climate Dyn.,* **36,** 289–308, doi:10.1007/s00382-009-0674-9.

Ferrari, R., J. C. McWilliams, V. M. Canuto, and M. Dubovikov, 2008: Parameterization of eddy fluxes near oceanic boundaries. *J. Climate,* **21,** 2770–2789.

Ferreira, D., J. Marshall, and P. Heimbach, 2005: Estimating eddy stresses by fitting dynamics to observations using a residual-mean ocean circulation model and its adjoint. *J. Phys. Oceanogr.,* **35,** 1891–1910.

Fox-Kemper, B., R. Ferrari, and R. Hallberg, 2008: Parameterization of mixed layer eddies. Part I: Theory and diagnosis. *J. Phys. Oceanogr.,* **38,** 1145–1165.

——, and Coauthors, 2011: Parameterization of mixed layer eddies. Part III: Implementation and impact in global ocean climate simulations. *Ocean Modell.,* **39,** 61–78, doi:10.1016/j.ocemod.2010.09.002.

Gent, P. R., and J. C. McWilliams, 1990: Isopycnal mixing in ocean circulation models. *J. Phys. Oceanogr.,* **20,** 150–155.

——, J. Willebrand, T. J. McDougall, and J. C. McWilliams, 1995: Parameterizing eddy-induced tracer transports in ocean circulation models. *J. Phys. Oceanogr.,* **25,** 463–474.

——, and Coauthors, 2011: The Community Climate System Model version 4. *J. Climate,* **24,** 4973–4991.

Griffies, S. M., 1998: The Gent–McWilliams skew flux. *J. Phys. Oceanogr.,* **28,** 831–841.

——, and K. Bryan, 1997: Predictability of North Atlantic multidecadal climate variability. *Science,* **275,** 181–184.

Guemas, V., and D. Salas-Melia, 2008: Simulation of the Atlantic meridional overturning circulation in an atmosphere–ocean global coupled model. Part I: A mechanism governing the variability of ocean convection in a preindustrial experiment. *Climate Dyn.,* **31,** 29–48, doi:10.1007/s00382-007-0336-8.

Hatun, H., A. B. Sando, H. Drange, B. Hansen, and H. Valdimarsson, 2005: Influence of the Atlantic subpolar gyre on the thermohaline circulation. *Science,* **309,** 1841–1844, doi:10.1126/science.1114777.

Hawkins, E., and R. Sutton, 2008: Potential predictability of rapid changes in the Atlantic meridional overturning circulation. *Geophys. Res. Lett.,* **35,** L11603, doi:10.1029/2008GL034059.

Holland, M. M., D. A. Bailey, B. P. Briegleb, B. Light, and E. Hunke, 2012: Improved sea ice shortwave radiation physics in CCSM4: The impact of melt ponds and aerosols on Arctic sea ice. *J. Climate,* **25,** 1413–1430.

Hurrell, J. W., and Coauthors, 2006: Atlantic climate variability and predictability: A CLIVAR perspective. *J. Climate,* **19,** 5100–5121.

Johns, W. E., and Coauthors, 2011: Continuous, array-based estimates of Atlantic Ocean heat transport at 26.5°N. *J. Climate,* **24,** 2429–2449.

Knight, J. R., C. K. Folland, and A. A. Scaife, 2006: Climate impacts of the Atlantic multidecadal oscillation. *Geophys. Res. Lett.,* **33,** L17706, doi:10.1029/2006GL026242.

Kushnir, Y., 1994: Interdecadal variations in North Atlantic sea surface temperature and associated atmospheric conditions. *J. Climate,* **7,** 141–157.

Kwon, Y.-O., and C. Deser, 2007: North Pacific decadal variability in the Community Climate System Model version 2. *J. Climate,* **20,** 2416–2433.

——, and C. Frankignoul, 2012: Stochastically-driven multidecadal variability of the Atlantic meridional overturning circulation in CCSM3. *Climate Dyn.,* **38,** 859–876, doi:10.1007/s00382-011-1040-2.

Large, W. G., and S. G. Yeager, 2009: The global climatology of an interannually varying air–sea flux data set. *Climate Dyn.,* **33,** 341–364, doi:10.1007/s00382-008-0441-3.

——, J. C. McWilliams, and S. C. Doney, 1994: Oceanic vertical mixing: A review and a model with a nonlocal boundary layer parameterization. *Rev. Geophys.,* **32,** 363–403.

Lawrence, D. M., K. W. Oleson, M. G. Flanner, C. G. Fletcher, P. J. Lawrence, S. Levis, S. C. Swenson, and G. B. Bonan, 2012: The CCSM4 land simulation, 1850–2005: Assessment of surface climate and new capabilities. *J. Climate,* **25,** 2240–2260.

Levitus, S., T. Boyer, M. Concright, D. Johnson, T. O'Brien, J. Antonov, C. Stephens, and R. Garfield, 1998: *Introduction.* Vol. 1, *World Ocean Database 1998,* NOAA Atlas NESDIS 18, 346 pp.

Medhaug, I., and T. Furevik, 2011: North Atlantic 20th century multidecadal variability in coupled climate models: Sea surface temperature and ocean overturning circulation. *Ocean Sci. Discuss.,* **8,** 353–396, doi:10.5194/osd-8-353-2011.

Mignot, J., and C. Frankignoul, 2005: The variability of the Atlantic meridional overturning circulation, the North Atlantic Oscillation, and the El Niño–Southern Oscillation in the Bergen Climate Model. *J. Climate,* **18,** 2361–2375.

Msadek, R., K. W. Dixon, T. L. Delworth, and W. Hurlin, 2010: Assessing the predictability of the Atlantic meridional overturning circulation and associated fingerprints. *Geophys. Res. Lett.,* **37,** L19608, doi:10.1029/2010GL044517.

Pohlmann, H., M. Botzet, M. Latif, A. Roesch, M. Wild, and P. Tschuck, 2004: Estimating the decadal predictability of a coupled AOGCM. *J. Climate,* **17,** 4463–4472.

Price, J., and J. Yang, 1998: Marginal sea overflows for climate simulations. *Ocean Modeling and Parameterization,* E. P. Chassignet and J. Verron, Eds., Kluwer Academic, 155–170.

Robson, J. I., 2010: Understanding the performance of a decadal prediction system. Ph.D. thesis, University of Reading, 233 pp.

——, R. Sutton, K. Lohmann, and D. Smith, 2012: Causes of the rapid warming of the North Atlantic Ocean in the mid-1990s. *J. Climate,* **25,** 4116–4134.

Schlesinger, M. E., and N. Ramankutty, 1994: An oscillation in the global climate system of period 65–70 years. *Nature,* **367,** 723–726.

Smith, R. D., and Coauthors, 2010: The Parallel Ocean Program (POP) reference manual, ocean component of the Community Climate System Model (CCSM). Los Alamos National Laboratory Tech. Rep. LAUR-10-01853, 141 pp. [Available online at http://www.cesm.ucar.edu/models/cesm1.0/pop2/doc/sci/POPRefManual.pdf.]

Steele, M., R. Morley, and W. Ermold, 2001: PHC: A global ocean hydrography with a high quality Arctic Ocean. *J. Climate,* **14,** 2079–2087.

Sutton, R. W., and D. L. R. Hodson, 2005: Atlantic Ocean forcing of North American and European summer climate. *Science,* **309,** 115–118.

Teng, H., G. Branstator, and G. A. Meehl, 2011: Predictability of the Atlantic overturning circulation and associated surface patterns in two CCSM3 climate change ensemble experiments. *J. Climate,* **24,** 6054–6076.

Yeager, S. G., and G. Danabasoglu, 2012: The sensitivity of Atlantic meridional overturning circulation variability to parameterized Nordic Sea overflows in CCSM4. *J. Climate,* **25,** 2077–2103.

——, A. Karspeck, G. Danabasoglu, J. Tribbia, and H. Teng, 2012: A decadal prediction case study: Late twentieth-century North Atlantic Ocean heat content. *J. Climate,* **25,** 5173–5189.

Zhang, R., and T. L. Delworth, 2006: Impact of Atlantic multidecadal oscillations on India/Sahel rainfall and Atlantic hurricanes. *Geophys. Res. Lett.,* **33,** L17712, doi:10.1029/2006GL026267.